

# Binary black hole evolutions of approximate puncture initial data

Tanja Bode,<sup>1</sup> Pablo Laguna,<sup>2</sup> Deirdre M. Shoemaker,<sup>2</sup> Ian Hinder,<sup>3</sup> Frank Herrmann,<sup>4</sup> and Birjoo Vaishnav<sup>5</sup>

<sup>1</sup>*Center for Gravitational Wave Physics*

*The Pennsylvania State University, University Park, PA 16802*

<sup>2</sup>*Center for Relativistic Astrophysics and School of Physics*

*Georgia Institute of Technology, Atlanta, GA 30332*

<sup>3</sup>*Max-Planck-Institut für Gravitationsphysik, Albert-Einstein-Institut, Golm, Germany*

<sup>4</sup>*Center for Scientific Computation and Mathematical Modeling,*

*University of Maryland, College Park, MD 20742*

<sup>5</sup>*Department of Physics and Astronomy*

*University of Texas At Brownsville, Brownsville, TX 77520*

Approximate solutions to the Einstein field equations are a valuable tool to investigate gravitational phenomena. An important aspect of any approximation is to investigate and quantify its regime of validity. We present a study that evaluates the effects that approximate puncture initial data, based on *skeleton* solutions to the Einstein constraints as proposed by Faye et al. [1], have on numerical evolutions. Using data analysis tools, we assess the effectiveness of these constraint-violating initial data and show that the matches of waveforms from skeleton data with the corresponding waveforms from constraint-satisfying initial data are  $\gtrsim 0.97$  when the total mass of the binary is  $\gtrsim 40M_{\odot}$ . In addition, we demonstrate that the differences between the skeleton and the constraint-satisfying initial data evolutions, and thus waveforms, are due to negative Hamiltonian constraint violations present in the skeleton initial data located in the vicinity of the punctures. During the evolution, the skeleton data develops both Hamiltonian and momentum constraint violations that decay with time, with the binary system relaxing to a constraint-satisfying solution with black holes of smaller mass and thus different dynamics.

PACS numbers:

## I. INTRODUCTION

With the developments of the past few years, numerical relativity simulations of binary black hole (BBH) systems from inspiral to merger are now feasible, almost routine. Most importantly, they are quickly becoming a potent tool to study highly relevant astrophysical phenomena. Approximations such as those provided by post-Newtonian (PN) theory have also proven to be valuable tools. They have the appeal of avoiding the computational complexities associated with finding exact solutions to the Einstein field equations. As the demand for more efficient simulations increases, it is desirable to consider approximate methodologies in conjunction with numerical relativity approaches. A natural “marriage” in this regard, which is the focus of this work, is to consider full Einstein evolutions of approximately constraint-satisfying initial data.

In general relativity, constructing initial data requires solving the Einstein constraints, a coupled set of elliptic equations (see Baumgarte and Shapiro [2] for a review on the mathematical foundations of numerical relativity and Cook [3] for constructing initial data). Thus, in general obtaining solutions to the Einstein constraints necessitates solving elliptic equations, which is a complex numerical problem. When black hole (BH) excision is used, the solvers are non-trivial [4, 5, 6] because of the excision boundaries. Even without excision, developing constraint solvers is demanding [7] and often requires introducing simplifying assumptions such as spatial conformal flatness.

Flexibility is also a very important issue. The family of problems addressed by numerical relativity is quickly expanding, involving non-traditional BH systems beyond the two-body problem [8, 9]. Without modifications to the standard initial data methodology, there will be limitations on the class of problems one is able to consider.

The focus of the present work is on the full Einstein numerical evolution of constraint-violating or approximate initial data. Evolutions of constraint-violating BBH initial data have been considered in the past. They were mostly done in the context of superposed Kerr-Schild BHs [10, 11, 12, 13]. More recently, constraint-violating initial data for punctures has been used for multiple BH evolutions [8, 9].

The difference with previous studies is in the building blocks used to construct the data. In Refs. [8, 9, 14], the initial data sets were built from perturbative solutions of single punctures (boosted and/or spinning). Our approach, on the other hand, follows closely the *skeleton* solutions of the Einstein equations introduced by Faye et al. [1]. These solutions are derived from the full Arnowitt-Deser-Misner (ADM) Hamiltonian with the BHs represented by point-like sources modeled by Dirac delta function distributions. We consider configurations of non-spinning, equal-mass BBHs in quasi-circular orbits and investigate how well the evolution of these initial data is able to reproduce the corresponding results of constraint-satisfying initial data. We assess the effectiveness of the skeleton initial data by computing the matches with waveforms from constraint-satisfying initial data evolutions. We find that the differences in the evo-

lutions, and thus waveforms, are due to negative Hamiltonian constraint violations present in the skeleton initial data. We observe that, during the course of the evolution, the skeleton data develops both Hamiltonian and momentum constraint violations which both propagate away and decay over time while the binary system relaxes to a constraint-satisfying solution with BHs of smaller mass and thus different dynamics.

In Sec. II, we derive the procedure for constructing skeleton puncture initial data. In Sec. III, we focus on quasi-circular configurations of equal-mass, non-spinning BBHs, and, using the effective potential method [3], we compare binding energies between skeleton and corresponding constraint-satisfying initial data. In Sec. IV, we investigate the structure of the Hamiltonian constraint violations in the skeleton data. In Sec. V, we present results of the evolutions. Sec. VI presents an analysis of the nature of the constraint violations with a model involving a single puncture. In Sec. VII, we discuss the impact of using waveforms from skeleton evolutions on data analysis. Conclusions are given in Sec. VIII.

The numerical simulations and results were obtained with the MayaKranc infrastructure as described in Refs. [15, 16, 17, 18].

## II. SKELETON INITIAL DATA

The traditional approach to constructing initial data in numerical relativity involves specifying the pair  $\{\tilde{g}_{ij}, \tilde{K}_{ij}\}$ , where  $\tilde{g}_{ij}$  is the intrinsic 3-metric to a  $t = \text{constant}$  hypersurface  $\Sigma_t$ , and  $\tilde{K}_{ij}$  denotes its extrinsic curvature. We use the index convention that Latin indices in the first part of the alphabet denote 4-dimensional spacetime indices and those from the middle denote 3-dimensional spatial indices. The pair  $\{\tilde{g}_{ij}, \tilde{K}_{ij}\}$  must satisfy the Einstein constraint equations:

$$\tilde{R} + \tilde{K}^2 - \tilde{K}_{ij}\tilde{K}^{ij} = 16\pi\tilde{\rho} \quad (1)$$

$$\tilde{\nabla}_j\tilde{K}^{ij} - \tilde{\nabla}^i\tilde{K} = 8\pi\tilde{j}^i. \quad (2)$$

Equations (1) and (2) are respectively known as the Hamiltonian and momentum constraints. The operator  $\tilde{\nabla}_i$  denotes covariant differentiation with respect to  $\tilde{g}_{ij}$  and  $\tilde{R}_{ij}$  its associated Ricci tensor. We follow the notation  $\tilde{K} \equiv \tilde{g}^{ij}\tilde{K}_{ij}$  and  $\tilde{R} \equiv \tilde{g}^{ij}\tilde{R}_{ij}$ .

Although we are interested in vacuum spacetimes of BH systems, we have kept the matter sources  $\tilde{\rho}$  (total energy density) and  $\tilde{j}^i$  (momentum density). This is so we are able, as in Ref. [1], to represent the BHs as pointlike sources modeled with Dirac delta distributions.

The constraints Eqs. (1) and (2) yield four equations; there are, thus, eight freely specifiable pieces in the data  $\{\tilde{g}_{ij}, \tilde{K}_{ij}\}$ . These free data can be used to single out the physical system under consideration (e.g. orbiting binary BHs) as well as to simplify solving the Einstein constraints. An elegant approach to identify the four

pieces in  $\{\tilde{g}_{ij}, \tilde{K}_{ij}\}$  that are fixed from solutions to the constraints was given in York [19], based on work by Lichnerowicz [20] and others. The method is based on the following conformal transformations and tensorial decompositions:

$$\tilde{g}_{ij} = \psi^4 g_{ij} \quad (3)$$

$$\tilde{K}_{ij} = \tilde{A}_{ij} + \frac{1}{3}\tilde{g}_{ij}\tilde{K} \quad (4)$$

$$\tilde{A}^{ij} = \psi^{-10}A^{ij} \quad (5)$$

$$\tilde{K} = K \quad (6)$$

$$A^{ij} = A_*^{ij} + (\mathbb{L}W)^{ij}, \quad (7)$$

where  $\tilde{A}^i{}_i = A^i{}_i = 0$  and  $\nabla_i A_*^{ij} = 0$  with  $\nabla_i$  covariant differentiation with respect to the conformal metric  $g_{ij}$ . In the tensorial decomposition of  $A^{ij}$  given by Eq. (7),  $A_*^{ij}$  gives the transverse part of  $A^{ij}$ , with the longitudinal part given by

$$(\mathbb{L}W)_{ij} \equiv 2\nabla_{(i}W_{j)} - \frac{2}{3}g_{ij}\nabla_k W^k. \quad (8)$$

With the transformations Eqs. (3-7), the constraint Eqs. (1) and (2) become:

$$8\Delta\psi - \psi R - \frac{2}{3}\psi^5 K^2 + \psi^{-7}A_{ij}A^{ij} = -16\pi\psi^5\tilde{\rho} \quad (9)$$

$$(\Delta_L W)^i - \frac{2}{3}\psi^{-6}\nabla^i K = 8\pi\psi^{10}\tilde{j}^i, \quad (10)$$

with  $R$  the Ricci scalar associated with the conformal 3-metric  $g_{ij}$  and  $(\Delta_L W)^i \equiv \nabla_j(\mathbb{L}W)^{ij}$ .

At this point, we introduce the assumptions of conformal flatness  $g_{ij} = \eta_{ij}$  and vanishing of both  $K$  and  $A_*^{ij}$ . These assumptions exhaust the eight freely specifiable conditions at our disposal on  $\{\tilde{g}_{ij}, \tilde{K}_{ij}\}$ ; five are in  $g_{ij}$ , one in  $K$  and two in  $A_*^{ij}$ . The constraints then take the form:

$$\Delta\psi + \frac{1}{8}\psi^{-7}(\mathbb{L}W)^2 = -2\pi\psi^5\tilde{\rho} \quad (11)$$

$$(\Delta_L W)^i = 8\pi\psi^{10}\tilde{j}^i, \quad (12)$$

where  $(\mathbb{L}W)^2 \equiv (\mathbb{L}W)^{ij}(\mathbb{L}W)_{ij}$ . In the absence of matter sources, or if one sets  $\tilde{j}^i = \psi^{10}\tilde{j}^i$ , the constraints Eqs. (11) and (12) decouple. That is, one can solve first Eq. (12) for  $W^i$  and use this solution to solve Eq. (11) for  $\psi$ .

Following Ref. [1], with the help of the momentum constraint Eq. (12), we notice that

$$\begin{aligned} (\mathbb{L}W)^2 &= 2(\mathbb{L}W)^{ij}\nabla_i W_j \\ &= 2\nabla_i[(\mathbb{L}W)^{ij}W_j] - 2W_j\nabla_i(\mathbb{L}W)^{ij} \\ &= 2\nabla_i[(\mathbb{L}W)^{ij}W_j] - 16\pi\psi^{10}W_j\tilde{j}^j. \end{aligned} \quad (13)$$

Substitution of Eq. (13) into the Hamiltonian constraint Eq. (11) yields

$$\Delta\psi + \frac{1}{4}\psi^{-7}\nabla_i[(\mathbb{L}W)^{ij}W_j] = -2\pi[\psi^5\tilde{\rho} - \psi^3W_i\tilde{j}^i]. \quad (14)$$

We address now the matter sources. The stress-energy tensor for a set of non-interacting point-like particles with rest mass  $\mathcal{M}_A$ , 4-velocity  $U_A^a$ , and comoving number density  $\mathcal{N}_A$  is given by

$$T^{ab} = \sum_A \mathcal{M}_A \mathcal{N}_A U_A^a U_A^b, \quad (15)$$

where the sum is understood to run over all the particles. For each particle  $A$  located at  $x_A^i$ , the comoving number density is given by a  $\delta$ -function as

$$\begin{aligned} \mathcal{N}_A &= \int \frac{1}{\sqrt{-{}^{(4)}g}} \delta^4[x^a - x_A^a(\tau)] d\tau \\ &= \frac{1}{\alpha U_A^t \sqrt{g}} \delta^3[x^i - x_A^i(t)] \\ &= \frac{\delta_A}{\gamma_A \sqrt{g}}, \end{aligned} \quad (16)$$

with  ${}^{(4)}g$  the determinant of 4-dimensional spacetime metric,  $\delta_A \equiv \delta^3(x^i - x_A^i)$ ,  $\alpha$  the lapse function,  $\gamma_A = \alpha U_A^t = -N_a U_A^a$ , and  $N^a$  the future-directed unit normal to the hypersurface  $\Sigma_t$ . The stress-energy tensor can then be rewritten as

$$T^{ab} = \sum_A \frac{\mathcal{M}_A \delta_A}{\gamma_A \sqrt{g}} U_A^a U_A^b. \quad (17)$$

Given Eq. (17), the matter sources take the form:

$$\begin{aligned} \tilde{\rho} &= N_a N_b T^{ab} \\ &= \sum_A \frac{\mathcal{M}_A \gamma_A \delta_A}{\psi^6 \sqrt{\eta}}, \end{aligned} \quad (18)$$

and

$$\begin{aligned} \tilde{j}^a &= -\perp_b^a N_c T^{bc} \\ &= \sum_A \frac{\mathcal{M}_A \perp_b^a U_A^b \delta_A}{\psi^6 \sqrt{\eta}} \\ &= \sum_A \frac{P_A^a \delta_A}{\psi^{10} \sqrt{\eta}}, \end{aligned} \quad (19)$$

where we have used  $\sqrt{g} = \psi^6 \sqrt{\eta}$ ,  $g_{ab} = {}^{(4)}g_{ab} + N_a N_b$  and  $\perp_b^a = {}^{(4)}g^{ac} g_{cb}$ . In deriving Eq. (19), we have also introduced the spatial momentum vector  $P_A^a \equiv \mathcal{M}_A \psi^4 \perp_b^a U_A^b$ . The vector  $P^a$  is related to the spatial part of the 4-momentum  $p^a = \mathcal{M} U^a$  of the point-like particles by  $P^a = \psi^4 \perp_b^a p^b$ . Substitution of the source Eqs. (18) and (19) into Eqs. (12) and (14) yields

$$\Delta\psi + \frac{1}{4\psi^7} \nabla_i [(\mathbb{L}W)^{ij} W_j] = -2\pi \sum_A \frac{m_A \delta_A}{\sqrt{\eta}} \quad (20)$$

$$(\Delta_L W)^i = 8\pi \sum_A \frac{P_A^i \delta_A}{\sqrt{\eta}}, \quad (21)$$

where

$$m_A = \frac{\mathcal{M}_A \gamma_A}{\psi} - \frac{W_i P_A^i}{\psi^7}. \quad (22)$$

Bowen and York [21] found a solution to the momentum constraint as given by Eq. (21). The solution represent BHs with linear momentum  $P_A^i$  and is explicitly given as

$$W^i = - \sum_A \frac{1}{4r} (7P^i + n^i n_j P^j) \Big|_A \quad (23)$$

with  $n^i$  the unit normal of constant  $r$  spheres in flat space. In terms of Eq. (23),  $(\mathbb{L}W)^{ij}$  takes the form:

$$(\mathbb{L}W)^{ij} = \sum_A \frac{3}{2r^2} \left[ 2P^{(i} n^{j)} - (\eta^{ij} - n^i n^j) n_k P^k \right]_A \quad (24)$$

In Eqs. (23) and (24),  $r_A = \|x^i - x_A^i\|$ ,  $n_A^i = (x^i - x_A^i)/r_A$  with  $x_A^i$  the coordinate location of BH $_A$ . It can be shown that the total ADM linear momentum is  $P^i = \sum_A P_A^i$ .

We now turn our attention to the Hamiltonian constraint Eq. (20). As pointed out in Ref. [1], the term  $\psi^7 \nabla_i [(\mathbb{L}W)^{ij} W_j]$  in Eq. (20) is a ‘‘flesh’’ term that provides the field between the particles and has the following contribution to the Hamiltonian:

$$\int \frac{1}{\psi^7} \nabla_i [(\mathbb{L}W)^{ij} W_j] d^3x = -7 \int \frac{1}{\psi^8} (\mathbb{L}W)^{ij} W_j \nabla_i \psi d^3x.$$

The only approximation that goes into defining the skeleton initial data is to neglect the contribution from this term. With this approximation, the Hamiltonian constraint Eq. (20) reads:

$$\Delta\psi = -2\pi \sum_A \frac{m_A \delta_A}{\sqrt{\eta}} \quad (25)$$

with  $m_A$  given by Eq. (22). Notice that  $m_A$  is singular at  $x^i = x_A^i$  because  $\psi$  and  $W^i$  are singular at  $x_A^i$ . Following Ref. [1], we solve Eq. (25) by means of Hadamard’s ‘‘partie finie’’ procedure [22]; that is,

$$\begin{aligned} \psi &= 1 - 4\pi \Delta^{-1} \left( \sum_A \frac{m_A(x^i) \delta_A}{2\sqrt{\eta}} \right) \\ &= 1 - 4\pi \Delta^{-1} \left( \sum_A \frac{m_A^{(\text{reg})}(x_A^i) \delta_A}{2\sqrt{\eta}} \right) \\ &= 1 - 4\pi \sum_A \frac{m_A^{(\text{reg})}(x_A^i)}{2} \Delta^{-1} \frac{\delta_A}{\sqrt{\eta}} \\ &= 1 + \sum_A \frac{m_A^{(\text{reg})}}{2r_A}, \end{aligned} \quad (26)$$

where

$$m_A^{(\text{reg})} \equiv \frac{\mathcal{M}_A \gamma_A}{\Phi_A} - \frac{W_i^A P_A^i}{\Phi_A^7} \quad (27)$$

$$\Phi_A = 1 + \sum_{B \neq A} \frac{m_B^{(\text{reg})}}{2r_{AB}} \quad (28)$$

$$\gamma_A = \left[ 1 + \frac{P^i P_i}{\mathcal{M}^2 \Phi^4} \right]_A^{1/2} \quad (29)$$

$$W_i^A P_A^i = \sum_{B \neq A} \left( \frac{-1}{4r_{AB}} \right) [7 P_B^i P_i^A - (n_i^{AB} P_A^i)(n_i^{AB} P_B^i)], \quad (30)$$

with  $r_{AB} = \|x_A^i - x_B^i\|$  and  $n_{AB}^i = (x_A^i - x_B^i)/r_{AB}$ . The parameter  $m_A$  is commonly known as the *bare* mass of the BH. On the other hand,  $\mathcal{M}$  is known as the irreducible mass of the BH.  $\Phi_A$  is the regularized value of  $\psi(x_A^i)$ . In summary, the skeleton initial data  $\{\tilde{g}_{ij}, \tilde{K}_{ij}\}$  is then given by  $\tilde{g}_{ij} = \psi^4 \eta_{ij}$  and  $\tilde{K}_{ij} = \psi^{-2} (\mathbb{L}W)_{ij}$  with  $\psi$  given by Eq. (26) and  $(\mathbb{L}W)^{ij}$  given by Eq. (24).

For comparison, the exact or constraint-satisfying puncture initial data method [23] consists also of  $\tilde{g}_{ij} = \psi^4 \eta_{ij}$  and  $\tilde{K}_{ij} = \psi^{-2} (\mathbb{L}W)_{ij}$  with  $(\mathbb{L}W)^{ij}$  given by Eq. (24), but in this case

$$\psi = 1 + \sum_A \frac{m_A}{2r_A} + u, \quad (31)$$

with  $u$  a regular solution to

$$\Delta u + \frac{1}{8\psi^7} (\mathbb{L}W)^2 = 0. \quad (32)$$

### III. QUASI-CIRCULAR INITIAL DATA

We restrict our attention to initial data configurations representing two equal mass ( $\mathcal{M}_1 = \mathcal{M}_2 \equiv \mathcal{M}$ ,  $m_1^{(\text{reg})} = m_2^{(\text{reg})} \equiv m$ ), non-spinning BHs in quasi-circular orbits. That is  $P_1^i = -P_2^i \equiv P^i$ ,  $r_{12} = \|x_1^i - x_2^i\| \equiv d$ , and  $n_i^{12} P^i = 0$ . Under these assumptions:

$$\psi = 1 + \frac{m}{2r_1} + \frac{m}{2r_2} \quad (33)$$

where

$$m = \frac{\mathcal{M} \gamma}{\Phi} - \frac{7 P^2}{4 d \Phi^7} \quad (34)$$

$$\Phi = 1 + \frac{m}{2d} \quad (35)$$

$$\gamma = \left[ 1 + \frac{P^2}{\mathcal{M}^2 \Phi^4} \right]^{1/2}. \quad (36)$$

While deriving Eq. (34), we used that for circular orbits  $W_i P^i = 7 P^2 / (4d)$  with  $P^2 = P^i P_i = P^i P^j \eta_{ij}$  as can be seen from Eq. (30).

We focus now on the differences between the constraint-satisfying and skeleton initial data for quasi-circular sequences using the effective potential method [3]. The general idea of this method is to find configurations that satisfy the condition:

$$\left. \frac{\partial E_b}{\partial l} \right|_{M,J} = 0, \quad (37)$$

with  $E_b = E - M$  the binding energy of the system. The distance  $l$  is a measure of the proper separation between the BHs (e.g. horizon to horizon), and  $M = 2\mathcal{M}$  is the sum of the irreducible masses. The quantities  $E$  and  $J$  are respectively the total ADM mass and angular momentum of the system [24], which can be computed from:

$$E = -\frac{1}{2\pi} \oint_{\infty} \nabla_i \psi d^2 S^i \quad (38)$$

$$J_i = \frac{\epsilon_{ijk}}{8\pi} \oint_{\infty} x^j \tilde{K}^{kl} d^2 S_l. \quad (39)$$

It is not too difficult to show from Eq. (39) that, given  $\tilde{K}_{ij} = \psi^{-2} (\mathbb{L}W)_{ij}$ , the ADM angular momentum for binaries initially in quasi-circular orbits is  $J = dP$ . On the other hand, with  $\psi$  given by Eq. (33) the total ADM mass from Eq. (38) is given by the sum of the bare masses of the BHs, namely  $E = 2m$ ; thus, the binding energy becomes  $E_b = 2m - 2\mathcal{M}$ . The bare masses for the skeleton initial data are obtained by solving the implicit Eq. (34) using a Newton-Raphson method.

Figure 1 (top panel) shows the comparison of the binding energy  $E_b$  as a function of the total ADM angular momentum  $J$  between the constraint-satisfying initial data from Tichy and Brüggmann [25] (squares) and the skeleton initial data in this work (triangles). The lower panel in Fig. 1 shows the corresponding % relative difference between both results. Not surprisingly, as the binary separation increases (i.e. larger angular momentum), the differences diminish. For reference, the vertical lines denote the angular momentum for typical data sets considered in the literature: QC0 in Ref. [26], R1 in Ref. [27] and D10 in Ref. [25]. The differences in binding energy between the skeleton and the constraint-satisfying initial data are  $\sim 20\%$  for QC0,  $\sim 6\%$  for R1 and  $\sim 2\%$  for D10.

Table I provides the parameters of the initial configurations for both the skeleton and constraint-satisfying data sets. The cases of exact or constraint-satisfying initial data are labeled with the letter “e” and the corresponding skeleton or approximate case with the letter “a”.

As mentioned before, the only fundamental difference between the two initial data sets is in the conformal factor  $\psi$ . For the constraint-satisfying data set  $\psi$  is computed from Eq. (31) by solving the Hamiltonian constraint in the form given by Eq. (32) and for the skeleton the conformal factor  $\psi$  is constructed using Eq. (26). In Fig. 2, we show the relative difference  $\delta\psi/\psi = (\psi_a - \psi_e)/\psi_e$  from the two data along the axis joining the punctures

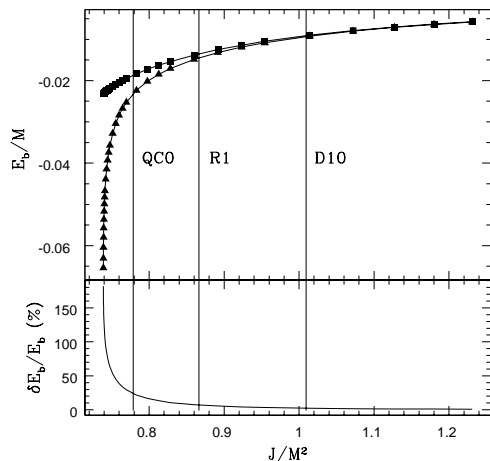


FIG. 1: Comparison of the binding energy  $E_b$  as a function of the total ADM angular momentum  $J$  between the initial data from Tichy and Brüggmann [25] (squares) and the skeleton initial data (triangles)

Run	$d/M$	$P/M$	$m/M$	$\mathcal{M}/M$	$E/M$	$J/M^2$
QC0e	2.337	0.33320	0.45300	0.519071	1.0195	0.7787
QC0a	2.337	0.33320	0.48950	0.519071	0.9790	0.7787
R1e	6.514	0.13300	0.48300	0.505085	0.9957	0.8664
R1a	6.514	0.13300	0.49717	0.505085	0.9943	0.8664
D10e	10.00	0.09543	0.48595	0.500000	0.9895	0.9530
D10a	10.00	0.09543	0.49458	0.500000	0.9891	0.9530

TABLE I: *Initial data parameters*: The punctures have bare masses  $m$ , linear momenta  $\pm P$  and are separated by a distance  $d$ . The irreducible mass of each BH from  $m^{(\text{reg})}$  is  $\mathcal{M}$ . The ADM masses and angular momenta of the spacetimes are given respectively by  $E$  and  $J$

( $x$ -axis) for the D10, R1 and QC0 cases. Notice the large differences in the immediate vicinity of the punctures. In the next section, we will investigate how these differences translate into constraint violations.

#### IV. HAMILTONIAN CONSTRAINT VIOLATIONS

For the remainder of the paper we will concentrate our attention on the D10 case: a situation in which the BHs are not too close to the merger and with an initial separation that permits a reasonable overlap with the post-Newtonian regime [28, 29]. It is important to point out that the numerical data D10e, although called exact, also violate the constraints initially. The violations

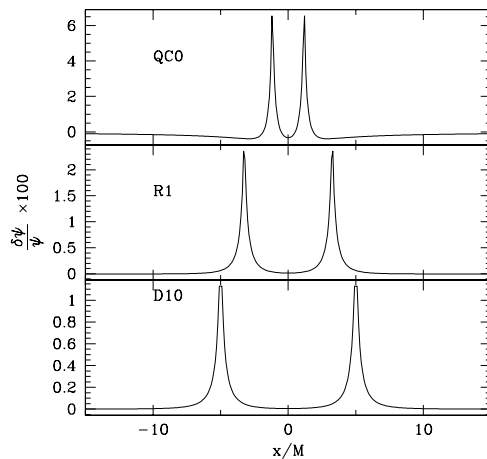


FIG. 2: The relative difference in the conformal factor  $\psi$  between the skeleton initial data and the corresponding constraint-satisfying data along the  $x$ -axis joining the punctures for the three cases labeled in Fig. 1.

in the exact initial data, however, are a consequence of numerical errors which can be made arbitrarily small in the limit to the continuum. On the other hand, the constraint violations in the skeleton data are independent of the resolution of the computational grid.

In order to understand the nature of the constraint violations in the skeleton initial data and in particular their dynamics in the course of the evolution, we take the point of view that the violations introduce “spurious” sources  $\tilde{\rho}$  and  $\tilde{j}^i$  in Eq. (1) and (2), respectively. Notice that initially we do not have a “spurious” momentum density  $\tilde{j}^i$  because the skeleton initial data by construction are an exact solution to the momentum constraint. It is important to keep in mind that one should not assign physical properties to  $\tilde{\rho}$  and  $\tilde{j}^i$ . They are only used to quantify constraint violations. In particular, the violations  $\tilde{\rho}$  are not restricted to satisfy energy conditions and thus are free to take negative values.

Fig. 3 shows a surface plot of  $\tilde{\rho}$  for the BBH skeleton initial data in the neighborhood of one of the punctures. Notice that the puncture seems to be embedded in a “cloud” or a pocket of negative  $\tilde{\rho}$ . Furthermore, the cloud is more negative in the direction aligned with the linear momentum of the puncture (in this case the  $y$ -axis). This effect is more evident from Fig. 4 where we plot  $\tilde{\rho}$  in the top panel along the  $x$ -axis (the direction joining the BHs) and in the bottom panel along the  $y$ -axis. The glitches at the bottom of the bottom of the constraint violation pockets are due to refinement boundaries.

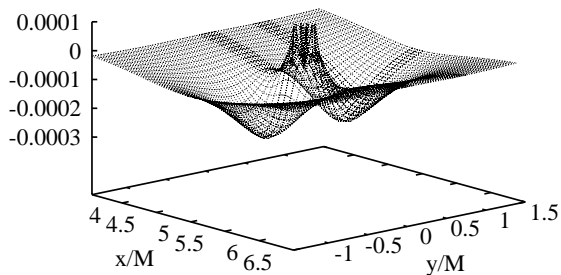


FIG. 3: Surface plot of  $\tilde{\rho}$ , as derived from the Hamiltonian constraint violations, in the  $xy$ -plane surrounding one puncture for the skeleton initial data, D10a.

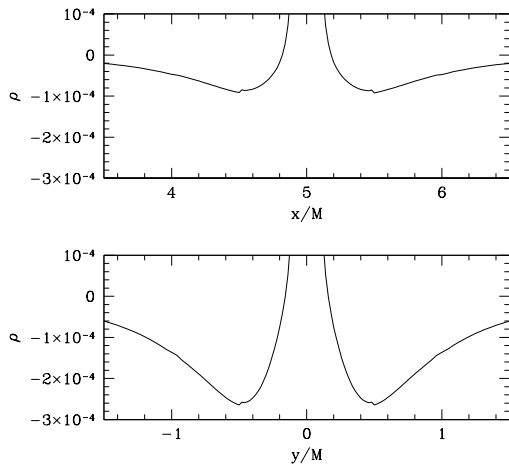


FIG. 4: Sources  $\tilde{\rho}$  corresponding to Fig. 3 along the  $x$ -axis joining the BHs (top panel) and along the  $y$ -axis (bottom panel), the linear momentum direction.

## V. SKELETON EVOLUTIONS

Given the initial data, we turn our attention now to evolutions. The evolution runs were done on a computational grid with 9 refinement levels, the finest 5 levels containing  $24^3$  gridpoints in radius and the remaining 4 with  $48^3$  gridpoints in radius. To check the dependence of the results with resolution, we considered grid spacings at the finest level of  $M/38.4$ ,  $M/44.8$  and  $M/51.2$ . The results presented here were done at the resolution of  $M/51.2$ .

Fig. 5 shows the trajectory of one of the BHs from the skeleton initial data (dashed line) as well as its constraint-

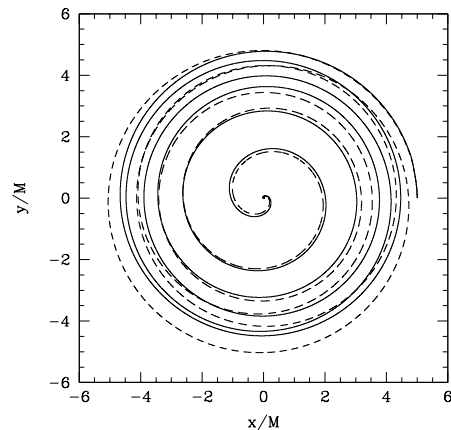


FIG. 5: Trajectory of one of the BHs from the skeleton initial data (dashed line) as well as its constraint-satisfying counterpart (solid line).

satisfying counterpart (solid line). Both trajectories are very close to each other during the first quarter orbit. Beyond that point, the BH from the skeleton initial data follows an eccentric orbit. Finally, near merger or at the plunge, the trajectories once again lie very closely together.

In Fig. 6, we compare the waveforms of the skeleton initial data with its constraint-satisfying counterpart as detected at  $50M$ . The presence of a phase shift between the two waveforms is evident. The constraint-satisfying initial data evolution reaches the merger approximately  $10M$  before the skeleton initial data evolution. This difference remains within  $1M$  of this between different resolutions. Another difference in the two evolutions is in the inspiral. As mentioned before, the skeleton data yields a larger eccentricity in the inspiral. This can be clearly observed from Fig. 7 where the same comparison as in Fig. 6 is shown but in terms of the amplitude (top panel) and phase (bottom panel). Here we have applied a time shift of  $10M$  to align the point at which the waveforms reach their maximum values. The inspiral and plunge of the binary is before the “knee” in the phase or the maximum in the amplitude. On the other hand the quasi-normal ringing of the final BH takes place after the knee in the phase and the maximum in the amplitude. Notice that the phases are practically identical for both cases. Furthermore, both the post-knee phase and post-maximum amplitude are almost the same for skeleton and constraint-satisfying evolutions, which is an indication that the final BHs are almost identical [30]. On the other hand, the inspiral amplitudes in Fig. 7 clearly show differences in the level of eccentricity as seen by the oscillations in the amplitude.

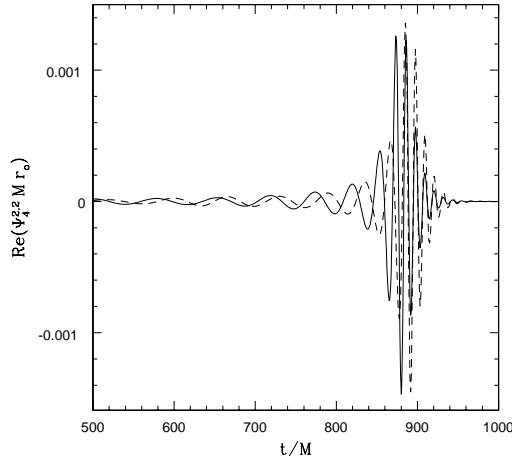


FIG. 6: Real parts of the waveform,  $r_o \Psi_4^{2,2} M$ , extracted at  $r_o = 50 M$  for both the skeleton (dashed line) and the constraint-satisfying (solid line) initial data.

From the waveforms, we have computed the energy  $E_{\text{rad}}$  and angular momentum  $J_{\text{rad}}$  radiated. For the constraint-satisfying initial data, we obtained  $E_{\text{rad}} = 0.0354 M$  and  $J_{\text{rad}} = 0.3060 M^2$  and for the skeleton data  $E_{\text{rad}} = 0.0359 M$  and  $J_{\text{rad}} = 0.3063 M^2$ , which correspond to differences of 1.4% and 0.1% respectively. These differences are consistent with differences in energy and angular momentum in the initial data ( $< 10^{-4}\%$ ).

To better understand the change in trajectories and the corresponding phase shift reflected in the waveforms (see Fig. 6), we have tracked the evolution of the apparent horizon (AH) masses. The AH mass for one of the BHs is plotted in Fig. 8 where the error due to grid spacing resolution is of order  $10^{-5} M$ . While the AH mass for the constraint-satisfying evolution stays relatively constant (solid line), the AH mass for the skeleton evolution varies significantly (dashed line). In fact, the mass starts more than 10% higher than the constraint-satisfying value and monotonically decreases. Empirically, the AH masses decrease as  $1/t$  at late times. By fitting a polynomial in  $1/t$  to the AH evolution at late times, we find the mass asymptotes to  $0.501 \pm 0.001 M$ , within 0.2% of the constraint-satisfying initial AH mass. However, the BHs merge before the skeleton AH mass could reach this asymptotic value. The differences and evolution of the AH masses early in the evolution of the skeleton data are consistent with the picture of a binary whose masses and therefore binding energy and dynamics are altered.

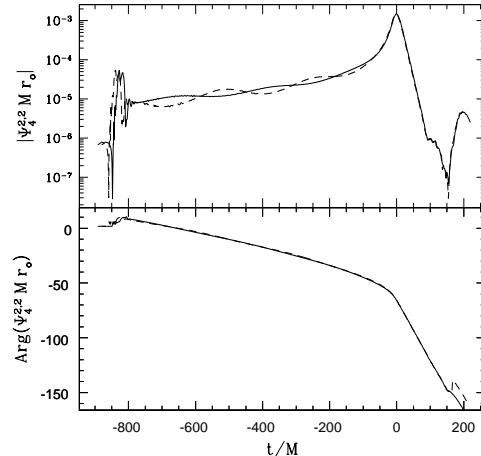


FIG. 7: Amplitude (top panel) and phase (bottom panel) of the waveforms  $r_o \Psi_4^{2,2} M$  in Fig. 6, skeleton data (dashed line) and constraint-satisfying data (solid line). The time axis has been shifted by  $10 M$  to align the point at which the amplitudes reach their maximum values.

## VI. SINGLE PUNCTURE ANALYSIS

As noted in Sec. III, the Hamiltonian constraint violations are negative in the vicinity of the punctures. To better understand the evolutions of the skeleton initial data, we consider a test case where we evolve a single, non-spinning puncture and add by hand negative constraint violations surrounding it. That is, we solve the Hamiltonian constraint as if there were an additional matter field  $\tilde{\rho}$  present, namely

$$\Delta\psi = -2\pi\tilde{\rho}\psi^5. \quad (40)$$

In order to guarantee the existence of a solution as discussed in [19, 31], if  $\tilde{\rho} > 0$ , one needs to re-scale the source according to the conformal rescaling  $\tilde{\rho} = \rho\psi_o^{-s}$ , with  $s > 5$ . In our case, however, we are mostly interested in  $\tilde{\rho} < 0$ , which does not require any rescaling for existence of a solution.

Following the procedure for multiple BHs, see Eq. (31), we use the ansatz  $\psi = \psi_o + u$ , with  $\psi_o = 1 + m/2r$  the solution to the homogeneous equation (i.e. the single puncture solution). With this ansatz, Eq. (40) becomes

$$\Delta u = -2\pi\rho(\psi_o + u)^n \quad (41)$$

where  $n = -3$  for  $\tilde{\rho} > 0$  and  $n = 5$  for  $\tilde{\rho} < 0$ .

For simplicity, we choose

$$\rho = \psi_o^m F e^{-(r-r_o)^2/(2\sigma^2)} \quad (42)$$

where  $r_o$  is the position with respect to the puncture and  $m = 0$  for  $\tilde{\rho} > 0$  and  $m = -5$  for  $\tilde{\rho} < 0$ . The factor  $\psi_o^m$  is

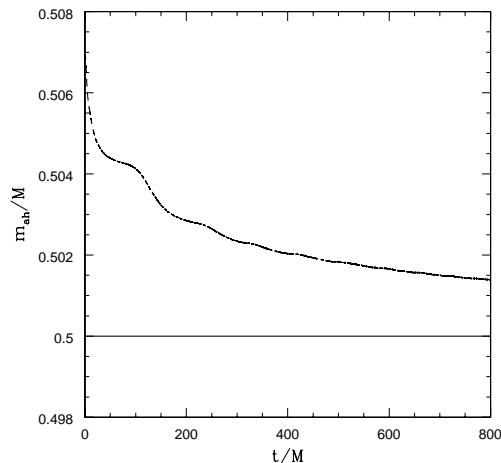


FIG. 8: The evolution of the AH mass of one of the BHs shown for both the constraint-satisfying initial data D10e (solid line) and its skeleton counterpart (dashed line). Errors in AH due to grid spacing are of order  $10^5 M$ .

Model	$F/M^2$	$E/M$	$\mathcal{M}_{AH}^i/M$	$\mathcal{M}_{AH}^f/M$	$E_\rho/M$
$F_1$	0.001	1.0046	1.0012	1.0041	0.0034
$F_2$	-0.001	0.9902	0.9973	0.9911	-0.0071
$F_3$	-0.010	0.9102	0.9858	0.9183	-0.0756

TABLE II: *Models*: Results of evolutions a single puncture in the presence of a Gaussian source  $\rho$  with  $r_o = \sigma = 1 M$  and amplitude  $F$ . The initial AH mass and ADM energy are  $\mathcal{M}_{AH}^i$  and  $E$  respectively. The AH mass at the end of the simulation is given by  $\mathcal{M}_{AH}^f/M$ , and  $E_\rho = E - \mathcal{M}_{AH}^i$ .

necessary for regularity of the solution  $u$  at the puncture. We also assume that the source  $\tilde{\rho}$  does not have initial momentum (i.e.  $\tilde{j}^i = 0$ ); thus, the momentum constraint remains satisfied as in the vacuum case.

Table II lists the results from the evolutions for  $r_o = \sigma = 1 M$ . Notice that model  $F_1$  has a positive source (i.e.  $F > 0$ ) and the other two have negative Hamiltonian constraint violations. The effect of the source  $\rho$  is evident in the ADM mass ( $E$ ) and initial AH mass ( $\mathcal{M}_{AH}^i$ ). For the positive source, the masses are larger than the puncture mass in vacuum,  $1 M$ , and smaller for the negative sources. Also in Table II, we include  $E_\rho = E - \mathcal{M}_{AH}^i$ , which gives a measure of the extra energy content in the initial data due to  $\rho$ .

We evolved the models in Table II for  $300 M$ . Fig. 9 shows how the AH mass evolves during the evolution. We have evolved the model  $F_3$  at different resolutions and estimated the AH masses to have an approximate relative error of  $\sim 0.002\%$ . We observed that at late

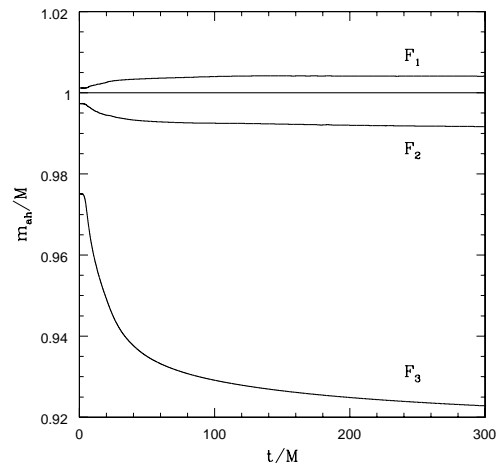


FIG. 9: Evolution of the AH mass for the models described in Table II. The error between resolutions for  $F_3$  was of order  $10^{-5}$  over the course of the evolution.

times the AH mass evolves as  $\mathcal{M}_{AH}^f + C/t$ . The values reported in Table II are those extrapolated to  $t \rightarrow \infty$ .

The evolutions of the single puncture models clearly demonstrate that depending on the signature of  $\rho$ , the mass of the BH, as measured from the AH, will increase or decrease. That is, over the course of the evolution, the AH masses evolve to approach the ADM energy, decreasing for a negative  $\rho$  and increasing for positive  $\rho$ . In other words, the source  $\tilde{\rho}$  initially hovering near a puncture will fall into the BH, increasing or decreasing its mass as the system becomes stationary depending on the sign of  $\tilde{\rho}$ . The extent to which the final mass of the BH approaches the total ADM energy depends on how much of the density  $\rho$  is “accreted” by the BH. Since in our case, we do not impose the restriction of positivity on  $\rho$ , the BH is free to decrease its mass. Notice also that the final AH mass does not satisfy the condition  $\mathcal{M}_{AH}^f = \mathcal{M}_{AH}^i + E_\rho$ , which means that a fraction ( $< 1\%$  in our cases) of  $E_\rho$  mass is radiated away. The choice of centering the Gaussian at  $r_o = 1 M$  was aimed at favoring the amount  $\tilde{\rho}$  accreted by the BH.

Figure 10 shows the Hamiltonian constraint violation  $\tilde{\rho}$  near the beginning of the simulation at  $t = 0.078 M$  (top panel) and at the end,  $t = 300 M$ , of the simulation (bottom panel). Solid lines represent the constraint-satisfying case and dashed lines the  $F_3$  model. Fig. 11 shows the corresponding results for the momentum constraint violations  $\tilde{j}^i$  along the  $x$ -axis. By construction, initially there are only Hamiltonian constraint violations in the  $F_3$  model. However, it is evident from the top panel in Fig. 11 that constraint violations in the momentum constraint develop also very early in the evolution. The growth of momentum constraint violations

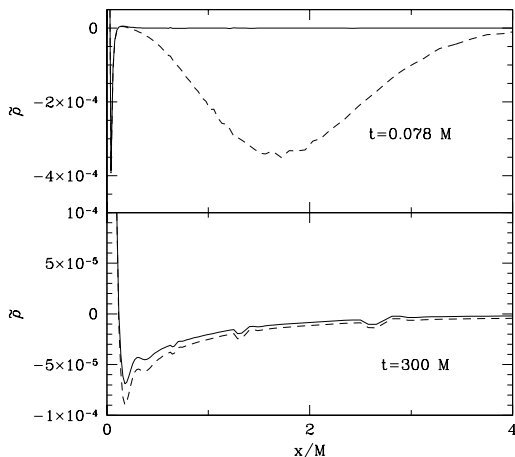


FIG. 10: Hamiltonian constraint violation  $\tilde{\rho}$  near the beginning of the simulation at  $t = 0.078 M$  (top panel) and at the end,  $t = 300 M$ , of the simulation (bottom panel). Solid lines represents the constraint-satisfying case and dashed lines the  $F_3$  model. The constraint violations still present at late times are due to discretization around the punctures.

proceed up to a time  $t \sim 3 M$ . The subsequent dynamics of the constraint violations consists of ingoing and outgoing waves. Because of the proximity to the puncture, the outgoing waves are a little bit weaker, with most of the constraint violations “accreted” by the BH. After approximately  $t \sim 50 M$  of evolution, the  $F_3$  model relaxes to the configuration of the constraint-satisfying puncture and remains there as seen in the bottom panels in Figs. 10 and 11. The final constraint violations in the system arise from numerical errors.

An important aspect to point out is that although the constraint-violating cases relax to a constraint-satisfying solution, the solutions that they relax to are not necessarily the same solutions as a single puncture in a vacuum spacetime. The new solution satisfies the Einstein equations but for a single puncture spacetime with a smaller mass. A similar situation occurs in the binary case; the system relaxes to a binary solution, but this solution is different than the vacuum case. The reason for this behavior is not currently understood.

## VII. IMPACT ON DATA ANALYSIS

Finally, we want to address the extent to which the waveforms from evolutions of skeleton initial data may be of use in exploring gravitational wave astronomy. We will focus on computing the matches between the skeleton and the constraint-satisfying waveforms. In principle, the match would be between the detector output,  $h_1$

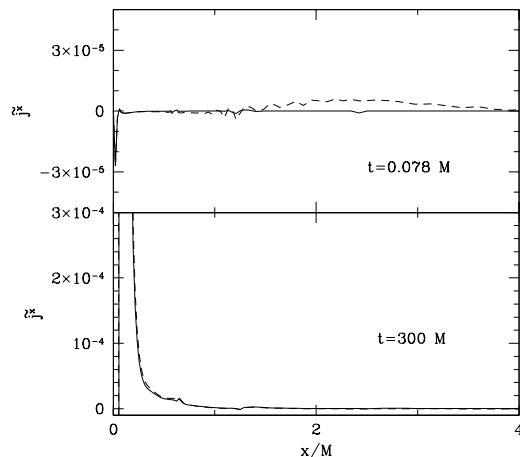


FIG. 11: Same as in Fig. 10 but for the momentum constraint violation  $\tilde{j}^x$ . The constraint violations still present at late times are due to discretization around the puncture.

and the template,  $h_2$ . Here  $h_1$  is the waveform from the constraint-satisfying evolution and  $h_2$  from the skeleton initial data evolution. Specifically, we will compare the waveforms using the minimax match given by [32, 33, 34].

$$\text{Match} \equiv \max_{t_0} \min_{\Phi_2} \max_{\Phi_1} \frac{\langle h_1 | h_2 \rangle}{\sqrt{\langle h_1 | h_1 \rangle \langle h_2 | h_2 \rangle}}, \quad (43)$$

where the inner product of two templates is defined by

$$\langle h_1 | h_2 \rangle = 4 \text{Re} \int_{f_{\min}}^{f_{\max}} \frac{\tilde{h}_1(f) \tilde{h}_2^*(f)}{S_h(f)} df. \quad (44)$$

The match is maximized over the time of arrival of the signal,  $t_0$ , and minimized/maximized over the initial phase,  $\Phi_1$  and  $\Phi_2$ , of the orbit when the signal/template enters the LIGO band. The variable  $S_h(f)$  denotes the noise spectrum for which we use the initial LIGO noise curve [35]. The domain  $[f_{\min}, f_{\max}]$  is determined by the detector bandwidth and the masses of our signal – set such that the initial frequency of the numerical waveform just enters the LIGO band. We have chosen to study the match for values of the total mass of the BBH system greater than  $20M_\odot$  because of the limited number of cycles that our waveforms include. A more detailed description of our calculation of the minimax match is given in [17].

The match between the constraint-satisfying and skeleton data versus mass is plotted in Fig. 12. As the total mass increases, the match between the waveforms increases, becoming  $> 0.99$  at  $60M_\odot$ . At such large total mass, the signal is dominated by the plunge and ring-down. Comparisons of the plunge and ring-down show

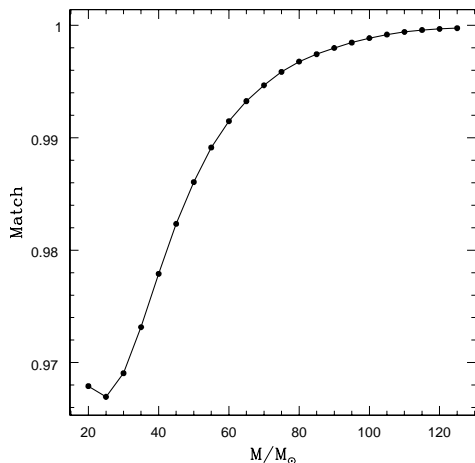


FIG. 12: Matches

(see Fig. 7) that the difference between the skeleton and constraint-satisfying evolution are very small. At masses lower than about  $40M_{\odot}$ , the match drops below 0.97 due to the difference in the binary dynamics prior to merger. We note that our calculation of match did not maximize over the mass of the two waveforms. Maximizing over the mass would have diminished the differences between the two waveforms.

### VIII. CONCLUSIONS

We have carried out a study of the evolution of skeleton, puncture BBH initial data as proposed by Faye et al. [1]. We focused on non-spinning punctures at initial separations of  $10M$ , where the difference in binding energy with the constraint-satisfying initial data is  $< 2\%$ . We showed that during the inspiral the skeleton data yields different dynamics; however, this difference significantly diminishes as the binary enters the plunge, merger and ring-down.

We tested the match between the constraint-satisfying and skeleton data for a series of total masses between  $20M_{\odot}$  and  $130M_{\odot}$ . Our results indicate that gravitational wave data analysis would have some tolerance for constraint-violating data, especially for those binaries in which the signal is plunge-merger dominated, as is the case of high mass BHs. We conclude that although the two systems were different, with one clearly violating the Einstein equations, the differences were not enough to im-

pact the match statistics for the mass ranges we included in our study and for the number of cycles present in our numerical waveforms. If these systems were evolved starting with a larger initial black-hole separation, the constraint violations would be smaller; and, therefore, the waveforms generated could be useful for detection over the complete BBH mass range for initial LIGO. If, however, larger constraint violations are present in the data that drive the early BH mass' lower, the differences may lead to errors in parameter estimation.

We also analyzed the impact of the Hamiltonian constraint violations. We showed that the main feature of the skeleton data is two packets of negative constraint violations in front of and behind the BH, along the direction of its momentum. We conjectured that these negative constraint violations acted as a source density that gets absorbed by the BHs during evolution. To test our conjecture, we considered a model consisting of a single, non-rotating puncture in which we artificially added a stationary Gaussian shell source that mimics the Hamiltonian constraint violations in the skeleton data. The evolutions of this single puncture model reproduce the decrease in the mass of the BH observed in the evolution of the skeleton data.

One remarkable aspect of our study is the ability of the BSSN equations and moving puncture gauges to evolve stably data away from the constraint surface. What is even more remarkable is how the evolution brings the data back to the Einstein constraint surface. We are currently investigating a broader class of solutions with this property.

In summary, our numerical evolutions show that the skeleton initial data proposed by Faye et al. [1] embeds the BHs in a “cloud” of negative constraint violations. These constraint violations act as a source field that when accreted by the BHs decreases their masses. The change in the masses modifies the binding energy of the binary and thus affects its orbital dynamics (e.g. adding eccentricity) but had little affect on the match of the two waveforms for initial LIGO for high mass black holes. The observed effects will decrease as the initial binary separation increases.

### Acknowledgments

This work was supported in part by NSF grants PHY-0354821, PHY-0653443, PHY-0244788, PHY-0555436, PHY-0801213 and PHY-0114375 (CGWP). Computations were performed at NCSA and TACC under allocation TG-PHY060013N. The authors thank M. Ansorg and E. Schnetter for contributions to the computational infrastructure.

[1] G. Faye, P. Jaranowski, and G. Schäfer, Phys. Rev. D **69**, 124029 (2004), arXiv:gr-qc/0311018.

[2] T. W. Baumgarte and S. L. Shapiro, Physics Reports

- 376**, 41 (2003), gr-qc/0211028.
- [3] G. B. Cook, *Living Rev. Rel.* **3**, 5 (2000), gr-qc/0007085.
- [4] J. Thornburg, in *The Ninth Marcel Grossman Meeting: On Recent Developments in Theoretical and Experimental General Relativity, Gravitation, and Relativistic Field Theories*, edited by V. G. Gurzadyan, R. T. Jantzen, and R. Ruffini (World Scientific, Singapore, 2003), pp. 1743–1744, gr-qc/0012012.
- [5] H. P. Pfeiffer, L. E. Kidder, M. A. Scheel, and S. A. Teukolsky, *Comput. Phys. Commun.* **152**, 253 (2003), gr-qc/0202096.
- [6] H. P. Pfeiffer, G. B. Cook, and S. A. Teukolsky, *Phys. Rev. D* **66**, 024047 (2002), gr-qc/0203085.
- [7] M. Ansorg, B. Brügmann, and W. Tichy, *Phys. Rev. D* **70**, 064011 (2004).
- [8] M. Campanelli, C. O. Lousto, and Y. Zlochower (2007), arXiv:0710.0879 [gr-qc].
- [9] C. O. Lousto and Y. Zlochower (2007), arXiv:0711.1165 [gr-qc].
- [10] U. Sperhake, B. Kelly, P. Laguna, K. L. Smith, and E. Schnetter, *Phys. Rev. D* **71**, 124042 (2005).
- [11] S. Brandt, R. Correll, R. Gómez, M. F. Huq, P. Laguna, L. Lehner, P. Marronetti, R. A. Matzner, D. Neilsen, J. Pullin, et al., *Phys. Rev. Lett.* **85**, 5496 (2000).
- [12] P. Marronetti, M. F. Huq, P. Laguna, L. Lehner, R. A. Matzner, and D. Shoemaker, *Phys. Rev. D* **62**, 024017 (2000), gr-qc/0001077.
- [13] R. A. Matzner, M. F. Huq, and D. Shoemaker, *Phys. Rev. D* **59**, 024015 (1999).
- [14] K. A. Dennison, T. W. Baumgarte, and H. P. Pfeiffer, *Phys. Rev. D* **74**, 064016 (2006), gr-qc/0606037.
- [15] F. Herrmann, I. Hinder, D. Shoemaker, and P. Laguna, *Class. Quant. Grav.* **24**, S33 (2007).
- [16] F. Herrmann, I. Hinder, D. Shoemaker, P. Laguna, and R. A. Matzner, *Astrophys. J.* **661**, 430 (2007).
- [17] B. Vaishnav, I. Hinder, F. Herrmann, and D. Shoemaker, *Phys. Rev. D* **76**, 084020 (2007).
- [18] F. Herrmann, I. Hinder, D. M. Shoemaker, P. Laguna, and R. A. Matzner, preprint (arXiv:0706.2541) (2007).
- [19] J. W. York, Jr., in *Sources of gravitational radiation*, p. 83 - 126 (1979), pp. 83–126.
- [20] A. Lichnerowicz, *J. Math Pures et Appl.* **23**, 37 (1944).
- [21] J. M. Bowen and J. W. York, *Phys. Rev. D* **21**, 2047 (1980).
- [22] P. Jaranowski and G. Schafer, *Phys. Rev. D* **61**, 064008 (2000), gr-qc/9907025.
- [23] S. Brandt and B. Brügmann, *Phys. Rev. Lett.* **78**, 3606 (1997), gr-qc/9703066.
- [24] J. M. Bowen and J. W. York, Jr., *Phys. Rev. D* **21**, 2047 (1980).
- [25] W. Tichy and B. Brügmann, *Phys. Rev. D* **69**, 024006 (2004), gr-qc/0307027.
- [26] M. Campanelli, C. O. Lousto, P. Marronetti, and Y. Zlochower, *Phys. Rev. Lett.* **96**, 111101 (2006).
- [27] J. G. Baker, J. Centrella, D.-I. Choi, M. Koppitz, and J. van Meter, *Phys. Rev. D* **73**, 104002 (2006).
- [28] J. G. Baker, J. R. van Meter, S. T. McWilliams, J. Centrella, and B. J. Kelly, *Phys. Rev. Lett.* **99**, 181101 (2007), gr-qc/0612024.
- [29] M. Hannam, S. Husa, U. Sperhake, B. Brügmann, and J. A. Gonzalez, *Phys. Rev. D* **77**, 044020 (2008), 0706.1305.
- [30] I. Hinder, B. Vaishnav, F. Herrmann, D. Shoemaker, and P. Laguna, *Phys. Rev. D* **77**, 081502 (2008), 0710.5167.
- [31] Y. Choquet-Bruhat, J. Isenberg, and J. W. York, *Phys. Rev. D* **61**, 084034 (2000).
- [32] L. S. Finn, *Phys. Rev. D* **46**, 5236 (1992).
- [33] B. Owen, *Phys. Rev. D* **53**, 6749 (1996).
- [34] T. Damour, B. R. Iyer, and B. S. Sathyaprakash, *Phys. Rev. D* **57**, 885 (1998).
- [35] A. Lazzarini and R. Weiss, *Tech. Rep. E950018-02-E* (1996).